# Interfacial Defect-Mediated Near-Infrared Silicon Photodetection with Metal Oxides

Jongbum Kim,[†,§] Lisa J. Krayer,[†,‡] Joseph L. Garrett,[†] and Jeremy N. Munday[*,†,‡,§]

[†]Institute for Research in Electronics and Applied Physics and [‡]Department of Electrical and Computer Engineering, University of Maryland, College Park, Maryland 20742, United States

[§]Department of Electrical and Computer Engineering, University of California, Davis, California 95616, United States

S Supporting Information

ABSTRACT: Due to recent breakthroughs in silicon photonics, sub-band-gap photodetection in silicon (Si) has become vital to the development of next-generation integrated photonic devices for telecommunication systems. In particular, photodetection in Si using complementary metal-oxide semiconductor (CMOS) compatible materials is in high demand for cost-effective integration. Here, we achieve broad-band near-infrared photo-detection in Si/metal-oxide Schottky junctions where the photocurrent is generated from interface defects induced by aluminum-doped zinc oxide (AZO) films deposited on a Si substrate. The combination of photoexcited carrier generation from both interface defect states and intrinsic Si bulk defect states contributes to a photoresponse of 1 mA/W at 1325 nm and 0.22 mA/W at 1550 nm with zero-biasing. From a fit to the Fowler equation for photoemission, we quantitatively determine the individual contributions from these effects. Finally, using this analysis, we demonstrate a gold-nanoparticle-coated photodiode that has three distinct photocurrent responses resulting from hot carriers in the gold, interface defects from the AZO, and bulk defects within the Si. The hot carrier response is found to dominate near the band gap of Si, while the interface defects dominate for longer wavelengths.

KEYWORDS: photodiode, interface defect, hot carrier, metal oxide, silicon photonics
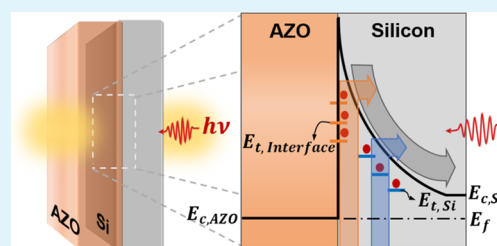
INTRODUCTION

Near-infrared (NIR) photodetection has attracted a great deal of attention for a broad range of applications including optical communications,[1,2] optical interconnects,[3,4] and energy conversion.[5,6] More specifically, NIR photodetection in Si photonics is essential for efficient optical to electrical conversion,[7] and therefore the demand has led to the development of photodetection techniques with numerous material platforms including germanium (Ge),[8] III−V compound semiconductors,[9] and silicon−germanium (SiGe).[10] Even though these approaches successfully provide efficient photodetection at telecommunication wavelengths, they have struggled with several practical issues such as incompatibility with complementary metal-oxide semiconductor (CMOS) technology, narrow bandwidth, and high manufacturing cost.[11,12]

Recently, hot-carrier-assisted photodetection in Si/metal junctions emerged as a promising approach to NIR photo-detection in Si with enhanced light absorption in the metal through the support of nanoscale antennas for plasmonic resonances[13−15] or thin metal films for Fabry−Pérot-like resonances.[16] Photodiodes with hot carrier injection from metal into Si have several technological advantages such as design flexibility on spectral selection and reduction of device size.[17] Nonetheless, nanoscale patterning of metal films is costly, time consuming, and generally not scalable for large-area devices, and so far, the Febry−Pérot resonant thin metal

films have low photoresponse at the wavelengths beyond 1.55 μm.

Alternatively, sub-band-gap Si photodetection can be obtained from defect-mediated absorption.[18] NIR photodiodes based on intrinsic bulk defects within the Si band gap by ion implantation or Au implantation have demonstrated the potential of defect-mediated photodetection systems;[19,20] however, the impact of surface or interface defect states on NIR photodetection in Si remains elusive. Defects introduced on the surface of Si by foreign atoms or deposited materials can modify the surface electronic states in Si, and those defects can contribute to carrier generation from sub-band-gap illumination.

Metal oxides known as transparent conducting oxides can be alternative metallic components for metal/Si Schottky junctions. They are widely used in optoelectronic devices due to their transparency in at visible wavelengths and their compatibility with standard CMOS fabrication procedures.[21] Even though the short mean free path of metal oxides (below 3 nm)[22] can limit the hot carrier injection from the metal oxides into Si, the tunable electrical and crystalline properties are promising for the development of NIR photodetectors with interfacial defect states at the Si surface.

In this work, we report sub-band-gap photodetection in lightly doped n-type silicon from interface defects induced by aluminum-doped zinc oxide (AZO) thin films. We observe a drastic enhancement of the photoresponsivity (PR) of photodiodes through the modification of the Schottky barrier (SB) and the density of interface defects introduced by controlling the material properties of AZO films. Particularly, we quantitatively distinguish the response from Si bulk defects and interface defects by fitting the photoresponse with the Fowler emission equation and confirm the role of interface defects for photoexcited carrier generation by exciting the epsilon near-zero (ENZ) mode in AZO thin films with the oblique incidence of p-polarized light. Finally, we design a photodiode with gold (Au) nanoparticles cladded with an AZO thin film to enhance the responsivity and to identify the impact of hot carrier injection from Au nanoparticles on the photodetection of Si/AZO Schottky junctions. Considering the numerous possible uses of metal oxides in optoelectronic and nanophotonic devices as conducting materials, plasmonic components, epsilon near-zero media, and active components, our work can make an enormous impact on the next generation of Si-photonic-based on-chip technologies.[21,23−28]

■ DISCUSSION

As sketched in Figure 1a, we present planar photodiode devices consisting of 50 nm thick AZO films deposited on n-
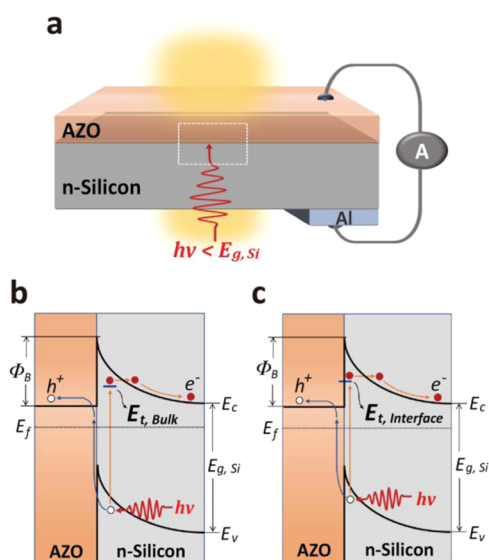
Figure 1. Device design and photoexcited carrier generation mechanism of a Si/AZO photodiode. (a) Schematic of a Si/AZO photodiode (out-of-scale for clarity). (b, c) Energy band diagram of Si/AZO Schottky junctions with two different sources for the generation of photoexcited carriers: (b) Si bulk defect states and (c) interface defect states. E_{vac}, E_c, E_v, E_f, and E_t refer to the energy of the vacuum level, the conduction band, the valence band, the Fermi level, and the defect state level, respectively.

type Si and an aluminum (Al) ohmic contact. The devices were fabricated in a simple four-step process: (1) removal of native oxide on Si, (2) deposition and annealing of an Al layer for the ohmic contact to Si, (3) removal of the resulting thermally grown oxide on Si, and (4) deposition of an AZO film with pulsed laser deposition (PLD). Further details are described in Methods. Figure 1b,c schematically illustrates the energy band diagram of Si/AZO Schottky junctions with two kinds of

defect trap states in the intrinsic Si bulk of the depletion region and at the AZO/Si interface, respectively. Sub-band-gap light ($h\nu < 1.1$ eV) illuminating the AZO through the Si substrate excites electrons from the valence band to available defect states, and the internal electric field from the upward band-bending in the depletion region forces the electrons to emit into the conduction band. Therefore, the SB (Φ_B) is a critical factor for determining the available energy states for photo-excited carriers, and it can be approximated using a modified Schottky−Mott relationship

$$\Phi_B = \chi_{AZO} - \chi_{Si}$$
$$= (\phi_{AZO} - \phi_{Si}) - (\Delta E_{c-f, AZO} - \Delta E_{c-f,Si}) \quad (1)$$

where $\chi_{Al:ZnO}$ is the electron affinity of AZO, χ_{Si} is the electron affinity of Si, ϕ_{Si} is the work function of Si, $\phi_{Al:ZnO}$ is the work function of AZO, $\Delta E_{c-f,Al:ZnO}$ is the electrochemical potential difference between the conduction band (E_c) and Fermi energy (E_f) in AZO, and $\Delta E_{c-f,Si}$ is the chemical potential difference between the conduction band (E_c) and Fermi energy (E_f) in Si. For simplicity of analysis, we ignore the potential of Fermi level pinning, which is usually observed in metal−semiconductor interface.[29]

To determine the impact of the SB on photoresponsivity (PR), we prepared five photodiodes with a 50 nm AZO layer deposited with varying PLD laser power densities to engineer the Si/AZO SB. The laser power density modifies the AZO material properties including the crystallinity and Al dopant concentration. The PLD laser intensity was 0.5, 0.7, 1.0, 1.3, and 1.5 mJ/cm^2, which corresponds to Al dopant concentrations of 1.2, 1.5, 1.7, 1.9, and 2.1 wt %, respectively (see Figure S1 for EDS measurement). The deposition temperature was set to 400 °C. We first measured the work function difference between the AZO films and Si substrate ($\Delta qV_{KPFM} = \phi_{AZO} - \phi_{Si}$) using Kelvin probe force microscopy (KPFM), which is a versatile method to characterize the surface potential of diverse materials.[30−32] As shown in Figure 2a, the KPFM signal (qV_{KPFM}) corresponds to the chemical potential difference between the platinum (Pt) tip and the surface of the measured material ($qV_{KPFM} = \phi_{Pt} - \phi_{Si \text{ or } AZO}$). Figure 2b shows the spatially resolved KPFM maps for the five different AZO films and the Si surfaces in a 30 μm × 30 μm area. The KPFM signals were uniform over the Si and AZO surfaces with signal deviations of less than ±30 mV, which can be attributed to the signal noise and surface roughness (see Figure S2 for the histogram of KPFM signal).

Next, we calculated both $\Delta E_{c-f,Si}$ and $\Delta E_{c-f,AZO}$ to estimate the SB from the measured ΔqV_{KPFM} (Figure 2c). $\Delta E_{c-f,Si}$ (=0.24 eV) was calculated from the Si resistivity ($\rho \approx 3\ \Omega$ m), and $\Delta E_{c-f,AZO}$ was estimated from the carrier densities of the AZO (n_{AZO}) films (see Methods for the calculation of n_{AZO}). The extracted n_{AZO} as a function of Al dopant concentration is plotted in Figure 2d. We observe that n_{AZO} is saturated above a 1.5 wt % Al dopant concentration because of Al dopant solid-solubility limits in ZnO, suggesting that the Fermi energy of 1.2 wt % AZO is lower than that of other AZO films. After compensating for the larger ΔE_{c-f} of the 1.2 wt % AZO, Figure 2c shows the calculated SB heights of the photodiodes (see SI for the calculation of ΔE_{c-f}). Notably, the SB of the photodiodes gradually increases as the dopant concentration is increased, and this relationship is verified by the decrease in reverse bias current with increasing dopant concentration
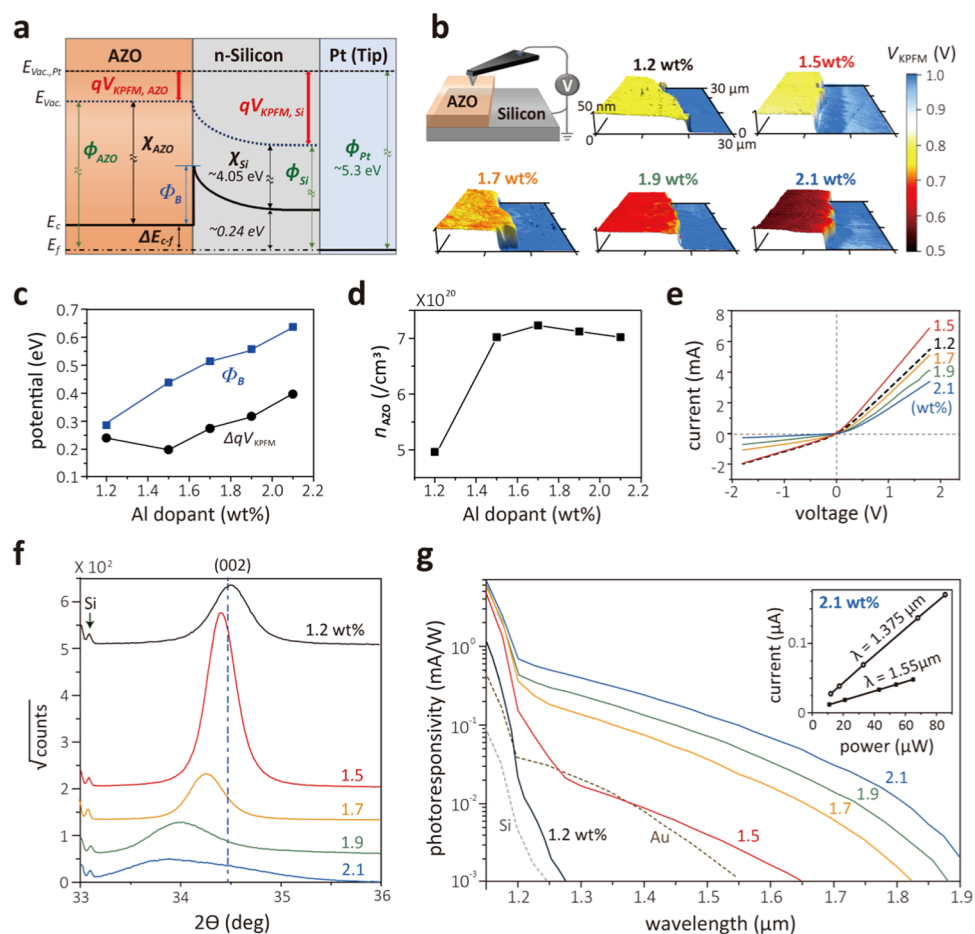
Figure 2. Performance characteristics of Si/AZO photodiodes with varying Al dopant concentrations. (a) Energy diagram of a Si/AZO Schottky junction and platinum (Pt) tip for KPFM characterization. KPFM measures the surface potential difference between Si and Pt ($qV_{KPFM,Si}$), and AZO and Pt ($qV_{KPFM,Si}$). (b) KPFM measurements on Si and AZO surfaces on photodiodes consisting of AZO with different doping concentrations (controlled by KrF excimer laser intensity for PLD growth) in a unit area of 30 μm × 30 μm. The KPFM signal is overlaid on the topography measurements of the Si substrate and AZO thin films. (c) Schottky barrier (Φ_B) of the Si/AZO junctions and the potential difference (ΔqV_{KPFM}) between AZO and Si. Schottky barriers are calculated by the Schottky–Mott rule from the measured KPFM signal. (d) Extracted carrier density of AZO as a function of Al dopant concentration. The charge carrier densities are determined by the Drude model of dielectric functions of AZO films. (e) Dark I–V curves of the Si/AZO photodiodes. The curve for 1.2 wt % AZO/Si photodiode is plotted with a dashed line for better comparison with 1.5 wt % AZO/Si data. (f) X-ray diffraction ($\omega - 2\theta$) patterns for AZO with varying Al dopant concentrations. (g) Spectral photoresponsivity of the Si/AZO photodiodes, bare Si, and a 50 nm-thick Au/Si photodiode. The inset is the photocurrent as a function of laser power at two different telecommunication wavelengths, 1.375 and 1.55 μm.

shown in the current–voltage (I–V) measurements in Figure 2e.

X-ray diffraction (XRD) measurements were used to determine an explanation for the change in the SB with dopant concentration. As shown in Figure 2f, the XRD peak is shifted to a lower angle with increasing dopant concentration. This behavior indicates that the electron band structure of AZO is modified by the planar stress and expansion of crystal lattice with increased dopant concentrations, resulting in the change of the energy level of the conduction band or band-gap renormalization.[33−36] Furthermore, increasing the PLD laser intensity during film growth, which can induce point defects at the AZO/Si interface such as interstitial Zn, can cause a band hybridization.[37,38]

Figure 2g shows the spectral photoresponse of the Si/AZO photodiodes under NIR illumination compared to those of the bare Si and Si/50 nm-thick Au films (see Methods for characterization details). As the Al dopant concentration increases, the PR of the Si/AZO photodiodes is drastically enhanced and extended well into the sub-band-gap regime of silicon, to at least 1.9 μm. In comparison, there is no sub-band-gap response from the bare Si, and the photoresponse of Si/Au photodiode vanishes near the wavelength of 1.55 μm. Note that the maximum photoresponse and device bandwidth of the Si/AZO devices increase with increasing SB; this is in contrast with the photocurrent generated from the internal photo-emission of a traditional hot-carrier-based Schottky photo-diode.[39] This result suggests that the increase of the SB enhances the strength of the internal electrical field and increases the available defect states at both the interface and bulk Si due to the extended width of the depletion region. The linear power dependence of photocurrent, shown in the inset of Figure 2g, verifies that the photoexcited carrier generation in the devices is not the result of nonlinear transitions such as carrier multiplication and two-photon absorption (TPA).[13,20]

To determine the sources of light absorption contributing to the carrier generation, we quantitatively compare a ratio of the PR and absorption (Ab) in the AZO, depletion region of Si,
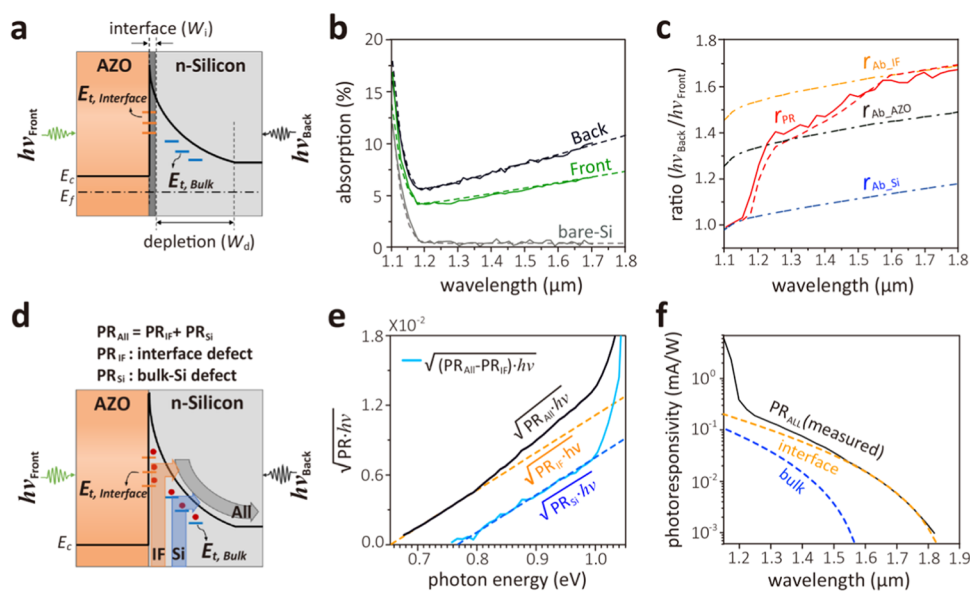
Figure 3. Decomposition of photoresponsivity (PR) in the 1.7 wt % Si/AZO photodiode. (a) Schematic illustrating the illumination direction and the spatial regions at the interface. The interface (W_i) is defined as a 2 nm depth from AZO/Si surface, and depletion width (W_d) is calculated as 600 nm. $h\nu_{front}$ and $h\nu_{back}$ refer to the illumination from the frontside and backside of the device, respectively. (b) Experiment (solid) and simulated (dashed) absorption spectrum of bare Si and Si/AZO photodiodes under front- and back-illuminations. (c) Ratio of PR (r_{PR}) and the ratio of absorption in AZO (r_{Ab_AZO}), depletion region of Si (r_{Ab_Si}), and at the interface (r_{Ab_IF}) between front- and back-illuminations. A red dashed line is the calculated ratio of PR from its decomposed PR. (d) Schematic diagram for the flow of photoexcited carriers via the different defect states from the interface and bulk Si of the depletion region. The measured PR is the summation of the carrier generation from both sets of defect states. (e) Fowler yield and (f) corresponding PR of the Si/AZO photodiode. The measured PR (All) is fit to an orange straight line (IF) for the decomposition of PR from interface defects, and the subtracted PR ($PR_{all} - PR_{IF}$) is fit to a blue straight line (Si) for the decomposition of PR from bulk defects.

and interfacial regions (W_i is 2 nm depth from the Si surface) under front- and back-illuminations as depicted in Figure 3a. As shown in Figure 3b, the light absorption in the photodiode with 1.7 wt % AZO is monotonically increasing as a function of wavelength, while the bare Si substrate absorbs less than 1% in NIR spectral range. Using numerical simulations, we modeled the extinction coefficient (k) of the bulk Si substrate (see Figure S4). For interfacial regions, we assume that this region has a 10 times higher extinction coefficient than the bulk Si substrate because the surface of Si can have many defect states from broken bonds and introduced impurities, which can behave as scattering or absorbing centers for incident light.[40] The 10× higher extinction coefficient in the interfacial region is only an approximation, and it is estimated from the total absorption as shown in Figure S3b. The simulated absorption spectrum for each illumination direction (dotted lines in Figure 3b) is well matched with the experimental data, and we confirm that the AZO film dominantly absorbs the incident light, and Si absorbs less than 1% similar to bare Si (see Figure S4). Figure 3c shows the PR ratio (r_{PR}) of front- to back-illumination along with the calculated absorption ratio for the depletion region in Si (r_{Ab_Si}), AZO (r_{Ab_AZO}), and interfacial regions (r_{Ab_IF}). The depletion width (W_d) in Si is estimated as 600 nm from the Si surface using the equation $W_d = \sqrt{2\varepsilon_{si}\Phi_B/(qn_{si})}$, where ε_{si} is the dielectric constant of Si, and n_{si} is the carrier density of Si. From the resistivity measurement of Si, we calculate $n_{si} = 2 \times 10^{15}$ cm^{-3}. Below 1.15 μm of wavelength, r_{PR} is well matched with r_{Ab_Si}, suggesting that the photoexcited carriers are generated from the interband absorption in the Si substrate. However, r_{PR} abruptly increases at the wavelengths of 1.15 μm and it does not follow the trends of any of the absorption ratios for the

wavelength >1.15 μm. From this result, we assume that the carriers are generated from light absorption in multiple regions for longer wavelength illumination, namely, a combination of the interfacial region and depletion region as illustrated in Figure 3d.

According to the Fowler theory for photoemission, which quantifies the probability that a photoexcited carrier can be collected through a barrier in the presence of an electric field, there is a linear relationship between the Fowler yield ($\sqrt{PR \cdot h\nu}$) and photon energy, i.e., $\sqrt{PR \cdot h\nu} \propto (h\nu - \Phi_B)$.[41,42] From a fit to the Fowler yield for back-illumination, we observed that the PR can be decomposed into two distinct linear fits, suggesting that the PR is generated from two sources (Figure 3e). Because r_{PR} approaches r_{Ab_IF} for wavelengths >1.5 μm, the PR generated from the lower barrier energy ($E_t = 0.65$ eV) is likely from interface defects. After subtracting the fit to the Fowler equation for $E_t = 0.65$ eV from the PR, we extract the second linear response (blue solid line in Figure 3e), which corresponds to the photoexcited carriers via Si bulk defect states. The decomposed fits each have their own barrier energy ($E_{t,interface} = 0.65$ eV and $E_{t,Si} = 0.76$ eV), suggesting that the barrier is determined by the energy level of the defect state (E_t) available for the photoexcited carriers. The decomposed Fowler yields in Figure 3e can be converted to PRs as plotted in Figure 3f. Using the two different contributions to the PR obtained from the back-illumination experiment (Figure 3f), the PR with front-illumination (PR_F) can be calculated as $PR_F = PR_{B\_IF}/r_{Ab\_IF} + PR_{B\_Si}/r_{Ab\_Si}$, where PR_{B_IF} and PR_{B_Si} are the PR from the interfacial states and depletion states with back-illumination, respectively. The ratio of the calculated PR_F to PR_B (red dotted line in Figure 4b) is in good agreement to the measured r_{PR} (see Figure S5 for the cases with different Al
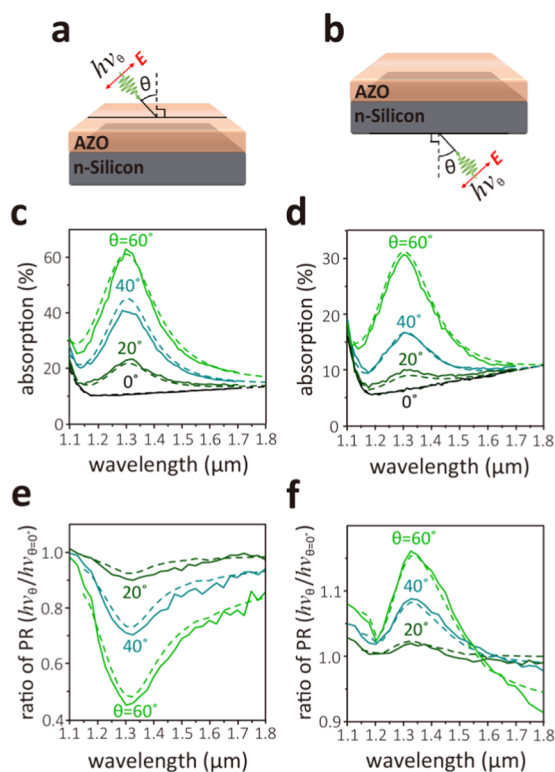
Figure 4. Absorption and photoresponse (PR) of the 1.7 wt % Si/AZO photodiode at the ENZ mode in the AZO film. Schematic illustrating the oblique incidence of p-polarized light from the (a) frontside and (b) backside of the photodiode. Absorption spectrum of the photodiode with different angles of incidence from the (c) frontside and (d) backside of the photodiode. The ratio of the PR at oblique incidence (θ) and normal incidence ($\theta = 0$) from the (e) frontside and (f) backside of the photodiode. The solid lines are experiment and the dashed lines are simulation.

dopant concentrations). Furthermore, the position of the energy levels of the interfacial defect states can explain the large jump in the photoresponse that occurs between samples with 1.5 and 1.7 wt % AZO (Figure 2). The SB in 1.5 wt % AZO is 0.44 eV, as shown in Figure 2c; hence, the defect states located at $E_{c,Si}$ −0.45 eV cannot be affected by the internal electrical field, resulting in the lower responsivity. However, for the defect states located above $E_{c,AZO}$, the photoexcited carriers at these defect states can be injected to Si.

We confirm our analysis by measuring the relationship between the PR and absorption at the ENZ mode of the AZO films. As displayed in Figure 4a,b, p-polarized light illuminated with an oblique incidence from the top or bottom direction enhances the absorption in AZO films due to the excitation of the ENZ mode.[43,44] Figure 4c,d shows the absorption of the 1.7 wt % AZO photodiode with front- and back-illuminations, respectively. Regardless of the direction of incidence, the absorption in the AZO is enhanced at the ENZ wavelength of AZO ($\lambda_{ENZ} = 1.3\ \mu m$) with an increasing angle of incidence. However, the ratio of the PR with oblique incidence (θ) to the PR with normal incidence ($\theta = 0$) under front-illumination gradually decreases as shown in Figure 4e, because of the decrease of absorption at the Si interface. The intensity of the PR was reduced 60%, while the absorption in AZO is enhanced 6 times at ENZ wavelength, verifying that the PR is not generated from photoexcited carriers in the AZO. Even though hot carrier excitation has been reported in metal

oxides,[45−48] it is expected that AZO has a prohibitively short mean free path, because of high scattering and recombination preventing photoemission from metal oxides.[49]

In contrast to the PR from front-illumination, the PR ratio for back-illumination increases at the ENZ wavelength as the incident angle increases (Figure 4f). When the angle of incidence becomes closer to Brewster's angle ($\theta_{Brewster} = 75°$) and the ENZ mode in the AZO is excited, the reflectivity of the Si/AZO interface increases, which, in turn, increases the absorption at both the Si/AZO interface and depletion region (see Figure S6). For both front- and back-illuminations, the estimated PR ratio of oblique incidence (θ) to normal incidence ($\theta = 0$) is in good agreement with the experimental data, confirming that the generation of photocurrent can be decomposed into two sources: interface states and Si trap states.

We further study the role of interface defects by fabricating photodiodes with AZO films deposited at different temperatures ranging from 200 to 600 °C with a constant PLD laser power of 1.5 mJ/cm^2. The SB of those devices was characterized using the same procedure stated above (see Figure S7 for carrier density). Figure 5a displays $\Delta q V_{KPFM}$ and the SB of the photodiodes. When varying the substrate temperature for a constant Al dopant concentration of 2.1 wt %, the variation of the SB (ranging from 0.55 to 0.65 eV) is comparably smaller than the previous results varying the dopant concentration. This result is consistent with the significantly smaller reverse bias (Figure 5b) compared to the photodiodes with lower Al dopant concentration. The shift in the XRD peaks measured from the AZO films (0.23°) shown in Figure 5c is also comparably smaller than the shift when varying the dopant concentration (0.67°), suggesting that the SB of a Si/AZO junction can be estimated by determining the peak position (lattice parameter) of AZO.

The PR of the constant dopant concentration photodiodes, shown in Figure 5d, notably decreases as the substrate temperature increases. The photodiode with AZO film deposited at 200 °C provides the highest responsivity corresponding to external quantum efficiencies (EQEs) of 8.7×10^{-4} and 1.8×10^{-4} for the wavelengths of 1325 and 1550 nm, respectively. This result is better than previously reported Au-implanted Si photodiode under five reverse bias, which has achieved the EQEs of 2.8×10^{-4} and 9.3×10^{-5} for the wavelengths of 1310 and 1550 nm, respectively.[20] The decrease in the PR is likely a result of changes in the number of interface defect states as the AZO changes from amorphous to crystalline with increasing substrate temperature. The disordered crystallinity of AZO introduces point defects such as interstitial Zn, oxygen vacancies, and excess Al dopant at the interface, increasing the available defect states for photoexcited carrier generation. Figure 5e illustrates the changes in the interfacial defect states for AZO films deposited at 200 and 600 °C. Even though the two samples have similar SB heights, the PR of the amorphous photodiode is roughly 3 times the PR of the crystalline photodiode at a wavelength of 1.55 μm, indicating that amorphous AZO induces more defects at the interface for sources of carrier emission.

Finally, we examine the performance of Si/AZO Schottky photodiodes when incorporating Au plasmonic nanoparticles to gain insight into the impact of hot carrier injection on the PR. Here, the PR is generated from a combination of hot carrier injection from the Au nanoparticles, interface defects from Si/AZO interface, and Si bulk defects of the depletion
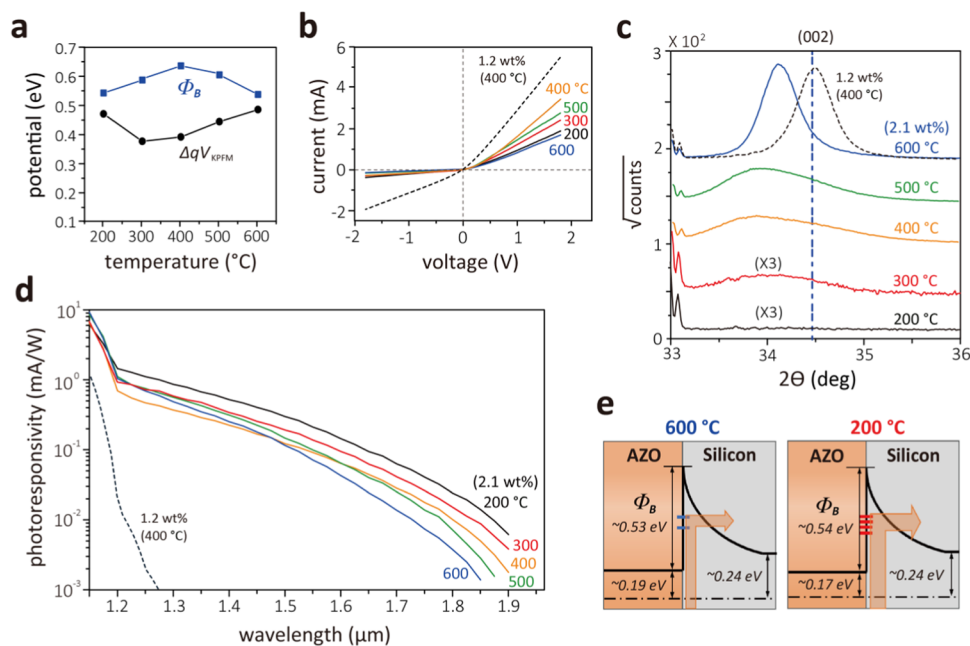
Figure 5. Performance characteristics of Si/AZO photodiodes with varying density of interface defect states. (a) Schottky barrier (Φ_B) of the Si/AZO junctions and the potential differences ($\Delta q V_{KPFM}$) between AZO and Si. The AZO films are deposited on Si at different substrate temperatures. (b) Dark $I{-}V$ curves of the photodiodes and (c) X-ray diffraction ($\omega - 2\theta$) patterns. The XRD signals of AZO film deposited at 200 and 300 °C are multiplied three times (×3) to more clearly show the peak position. (d) Spectral photoresponsivity of the Si/AZO photodiodes. (e) Schematic showing the impact of the density of interface defect states with similar Schottky barrier heights. The $I{-}V$ characteristic, XRD pattern, and photoresponsivity of the photodiode with the AZO film grown at 400 °C and 1.2 wt % Al dopant concentration are provided for comparison (dashed line in (b), (c), and (d)).

region in the Si. As shown in the SEM image in Figure 6a, we fabricated Au nanoparticles on a Si substrate by annealing 7 nm-thick Au films at 425 °C. The size of Au nanoparticles varies from 20 to 100 nm, and the Au nanoparticles cover 65% of the Si surface. Figure 6b shows the absorption of the Au nanoparticles on the Si substrate when illuminating from the backside. Compared to bare Si, Au nanoparticles enhance the absorption up to 1.7 μm. Figure 6c shows the calculated absorption, using finite difference time domain (FDTD, Lumerical) simulations, for nanoparticles ranging from 40 to 100 nm. The electric field profile of a nanoparticle with a diameter of 80 nm and a height of 30 nm at a wavelength of 1.2 μm shows enhanced fields at the base of the particle suggesting a localized surface plasmon (LSP) resonance. When the LSP decays, it generates a hot electron in the nanoparticle, which is then injected into the Si over the Au/Si SB. Because the particles are randomly distributed over the surface, we assume that the absorption from particles with different radii from 40 to 100 nm is equally contributed to the overall absorption. Therefore, we take an average on the simulated absorption spectrum of particles with different radii from 40 to 100 nm. The average absorption of Au nanoparticles with varying sizes are well matched with measured absorption.

After depositing a 50 nm AZO film at 200 °C with a 2.1 wt % dopant concentration, we measured the PR (Figure 6d) and found that the PR decays rapidly compared to the photodiode without Au nanoparticles. For a better understanding of this behavior, we decomposed the PR into three components using a similar procedure as the Si/AZO photodiodes (see Figure S8). Figure 6e,f shows the decomposed PRs with and without the Au nanoparticles, respectively. Considering that the PR of the Au thin-film photodiode shown in Figure 2g vanishes at ~1.55 μm, the decomposed PR, which vanishes at the

wavelength 1.51 μm, is assumed to be hot carrier injection from the Au nanoparticles. Therefore, the enhancement of the PR above 1.5 μm can be attributed to the additional carrier generation resulting from hot carrier injection from the Au particles, and the reduced PR below 1.5 μm is likely due to the decrease in the AZO/Si interfacial surface area. Additionally, we expect that the increase in PR contributed from bulk Si defects is due to the localized electric field enhancement around the Au nanoparticles. Consequently, as depicted in Figure 6g,h, the Au nanoparticles improve the responsivity below the Au/Si SB wavelength of 1.5 μm, but it is not beneficial for extending detection bandwidth.

■ CONCLUSIONS

We report sub-band-gap photodetection in Si/AZO Schottky junctions resulting from the interface and bulk Si defects. Through quantitative analysis, we determined the contribution of each source of carrier generation for NIR illumination and determined that the PR of the photodiodes can be controlled by modifying the SB and the density of interface defects. This work represents new approach to achieve high efficiency, sub-band-gap optoelectronic response in Si devices via engineering the interface defect states, which is scalable and compatible to CMOS technology. Furthermore, we find that low-temperature deposition for amorphous films increases the device response, suggesting that this is a promising approach for cost-effective manufacturing of NIR Si photodiodes. The Si/metal-oxide photodetectors can be further improved by optimizing the device architecture for CMOS integration. In addition, we can further improve the devices' performance by ion-implanting other materials to create additional deep-level interfacial defects and bulk defects for broadening the spectral range. Quantum well or gain media can also be embedded to achieve
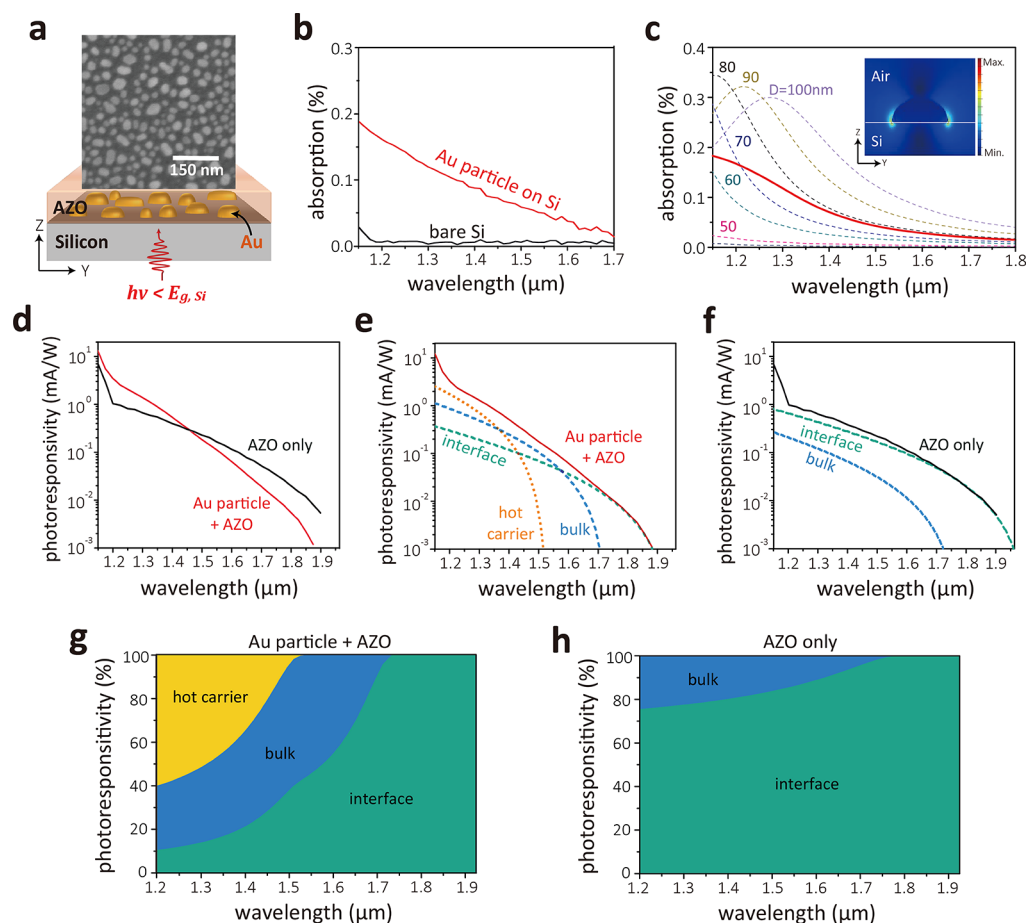
Figure 6. (a) SEM image and schematic of the Au nanoparticles embedded in the Si/AZO photodiodes. (b) Experimental absorption spectrum of bare Si and the Au nanoparticles on Si. (c) Simulation of the absorption in Au nanoparticles with a 30 nm height with diameters ranging from 50 to 100 nm. The red solid line is the average of the absorption spectrum of Au nanoparticles with different sizes. (d) Spectral photoresponsivity (PR) of the Si/AZO photodiode with and without Au nanoparticles. The decomposed PR of (e) the Au nanoparticles embedded within a Si/AZO photodiode and (f) the original Si/AZO photodiode without Au nanoparticles. The contribution of each source (hot carrier, interface defects, and bulk defects) to overall photoresponsivity in the Si/AZO photodiode (g) with Au nanoparticles and (h) without Au nanoparticles.

photocurrent multiplication by the avalanche effect. Therefore, further investigation is needed to determine a theoretical model for the light absorption near the interface where the photocurrent is generated to provide additional information such as the internal quantum efficiency (IQE) and a greater understanding of the defect energy states. A theoretical model would provide guidance for the design of materials to develop improved interface defect-mediated Si photodiodes. Fundamentally, Si/AZO photodiodes consume little energy due to zero-biasing; therefore, these photodiodes would be advantageous for use in energy-efficient optical interconnects in on-chip Si photonics in the telecommunication regime.

■ METHODS

Sample Preparation. All devices were fabricated on 300 μm-thick, double side-polished, ⟨100⟩ n-type silicon wafers (>2 Ω cm). The wafers were cleaned in buffered oxide etch (BOE) to remove the native oxide. To make the ohmic contacts to the Si substrate, 150 nm aluminum (Al) films were deposited, using electron beam evaporation, in a thin strip on the top surface of each device, using a shadow mask, and annealed at 425 °C in a forming gas of 96% Ar and 4% H$_2$. The annealed sample was cleaned with BOE again to remove the native oxide, which can be formed during annealing, using photoresist to protect the Al contact layer. Finally, 40−50 nm-thick aluminum-doped zinc oxide (AZO) films were deposited on the back

surface of the Si substrate with pulsed laser deposition (PLD). The substrate temperature and laser intensity were varied to control the properties of the films while the base pressure was controlled at 1 × 10^{-6} Torr. For the fabrication of the Au nanoparticles, we deposited a 7 nm Au film, using electron beam evaporation on the backside of a Si substrate after depositing the Al ohmic contact to the Si. The Au nanoparticles were formed during the Al anneal at 425 °C in a forming gas of 96% Ar and 4% H$_2$.

Optical Characterizations. The optical properties of the 50 nm-thick AZO films were characterized by variable angle spectroscopic ellipsometry (V-VASE, J.A. Woollam) in the optical bandwidth from 0.2 to 1.7 μm. The dielectric functions of the films were retrieved by fitting a Drude + Tauc−Lorentz oscillator model to the ellipsometry data. The ellipsometer was also employed to measure the absorption spectrum of each photodiode. For photocurrent measurement, specific wavelengths were selected from a supercontinuum source (Fianium WhiteLase) using an acousto-optic tunable filter (AOTF). A 1.1 μm longpass filter was used to measure the photoresponsivity from 1.1 to 1.2 μm, and a 1.2 μm longpass filter was used to measure the photoresponsivity from 1.2 to 1.9 μm to completely block the high-order harmonic radiation emitted from the AOTF. The photocurrent from the Si/AZO detectors was measured using an SR830 lock-in amplifier. The power incident on the sample was measured using a calibrated InGaAs photodiode to calculate the responsivity. The intensity of our laser source dropped sharply at 1.95 μm; therefore, we measured the PR of each device up to 1.9 μm to maintain a high signal-to-noise ratio (noise level ≈0.1 μA/W).

Calculation of Carrier Density of AZO (n_{AZO}). From the extracted dielectric functions of the AZO films, we calculated n_{AZO} from the plasma frequency (ω_p) fitting parameter in the Drude model using the equation $\omega_p^2 = e^2 n_{AZO}/(\varepsilon_0 \varepsilon_\infty m_e^* \ m_0)$, where ε_0 is the permittivity of free space, ε_∞ is the high-frequency dielectric constant, m_0 is the mass of an electron, and m_e^* is the effective mass of the electron. (See Figure S3 for the dielectric function of AZO films.)

KPFM Measurement. KPFM is a scanning probe method that measures surface potential by applying an AC voltage between the tip and the sample to generate a signal proportional to the DC voltage difference between them. A feedback loop then applies a bias to the probe to minimize the oscillation, and the bias is recorded to produce a map of the surface potential. Heterodyne KPFM is a variant that mixes the driving AC voltage with the mechanical oscillation of the cantilever to quickly image samples with high resolution. A Cypher AFM (Asylum Research) with HQ:CSC37/Pt probes was used to scan the KPFM signal. An AC voltage is applied to a conductive Pt probe, which, in turn, causes the probe to oscillate, generating a signal proportional to the difference between the voltage of the probe and the surface. An applied AC voltage of 5 V at a driving frequency of 392.37 kHz and a detection frequency of 196.68 kHz was used.

Simulations. We validated the experimental absorption spectra with numerical simulations using a commercially available software based on the finite element method (COMSOL Multiphysics, Wave Optics Module). The absorption calculation of the nanoparticle was simulated with finite difference time domain (FDTD, Lumerical) simulations.

■ ASSOCIATED CONTENT

Ⓢ Supporting Information

The Supporting Information is available free of charge at https://pubs.acs.org/doi/10.1021/acsami.9b14953.

EDS characterization of AZO thin films, a histogram of KPFM signal, calculation of the Fermi energy of the AZO thin films, modeling the absorption in the Si substrate, decomposition process of PR to determine the source of carrier generation, absorption profile at the ENZ mode, and decomposition of the PR from Au nanoparticles embedded a Si/AZO photodiode (PDF)

■ AUTHOR INFORMATION

Corresponding Author

*E-mail: jnmunday@ucdavis.edu.

ORCID Ⓘ

Lisa J. Krayer: 0000-0001-9133-226X
Jeremy N. Munday: 0000-0002-0881-9876

Author Contributions

J.N.M. and J.K. conceived the project. J.K. carried out the fabrication of the devices. J.K. and L.J.K. performed the photoresponse and I−V measurement, and J.K. and J.L.G. performed the Kelvin probe force microscopy measurements (KPFMs) with an atomic force microscope. J.N.M. oversaw the project and provided the facilities. All of the authors contributed to and approved the manuscript.

Notes

The authors declare no competing financial interest.

■ ACKNOWLEDGMENTS

■ REFERENCES

(1) Soref, R. Mid-Infrared Photonics in Silicon and Germanium. *Nat. Photonics* **2010**, *4*, 495.

(2) Ackert, J. J.; Thomson, D. J.; Shen, L.; Peacock, A. C.; Jessop, P. E.; Reed, G. T.; Mashanovich, G. Z.; Knights, A. P. High-Speed Detection at Two Micrometres with Monolithic Silicon Photodiodes. *Nat. Photonics* **2015**, *9*, 393.

(3) Pospischil, A.; Humer, M.; Furchi, M. M.; Bachmann, D.; Guider, R.; Fromherz, T.; Mueller, T. CMOS-Compatible Graphene Photodetector Covering All Optical Communication Bands. *Nat. Photonics* **2013**, *7*, 892.

(4) Chen, L.; Preston, K.; Manipatruni, S.; Lipson, M. Integrated GHz Silicon Photonic Interconnect with Micrometer-Scale Modulators and Detectors. *Opt. Express* **2009**, *17*, 15248−15256.

(5) Luque, A.; Martí, A. Towards the Intermediate Band. *Nat. Photonics* **2011**, *5*, 137.

(6) Luque, A.; Martí, A.; Stanley, C. Understanding Intermediate-Band solar Cells. *Nat. Photonics* **2012**, *6*, 146.

(7) Jalali, B.; Fathpour, S. Silicon Photonics. *J. Lightwave Technol.* **2006**, *24*, 4600−4615.

(8) Michel, J.; Liu, J.; Kimerling, L. C. High-Performance Ge-on-Si Photodetectors. *Nat. Photonics* **2010**, *4*, 527.

(9) Park, H.; W. Fang, A.; Jones, R.; Cohen, O.; Raday, O.; N. Sysak, M.; J. Paniccia, M.; E. Bowers, J. A hybrid AlGaInAs-Silicon Evanescent Waveguide Photodetector. *Opt. Express* **2007**, *15*, 6044−6052.

(10) Luryi, S.; Kastalsky, A.; Bean, J. C. New Infrared Detector on a Silicon Chip. *IEEE Trans. Electron Devices* **1984**, *31*, 1135−1139.

(11) Park, D. S.; Kim, K.; Pillans, B.; Lee, J.-B. Polydimethylsiloxane-Based Pattern Transfer Process for the Post-IC Integration of MEMS onto CMOS Chips. *J. Micromech. Microeng.* **2004**, *14*, 335−340.

(12) Eng, P. C.; Song, S.; Ping, B. State-of-the-Art Photodetectors for Optoelectronic Integration at Telecommunication Wavelength. *Nanophotonics* **2015**, *4*, 277.

(13) Knight, M. W.; Sobhani, H.; Nordlander, P.; Halas, N. J. Photodetection with Active Optical Antennas. *Science* **2011**, *332*, 702−704.

(14) Knight, M. W.; Wang, Y.; Urban, A. S.; Sobhani, A.; Zheng, B. Y.; Nordlander, P.; Halas, N. J. Embedding Plasmonic Nanostructure Diodes Enhances Hot Electron Emission. *Nano Lett.* **2013**, *13*, 1687−1692.

(15) Li, W.; Valentine, J. Metamaterial Perfect Absorber Based Hot Electron Photodetection. *Nano Lett.* **2014**, *14*, 3510−3514.

(16) Krayer, L. J.; Tennyson, E. M.; Leite, M. S.; Munday, J. N. Near-IR Imaging Based on Hot Carrier Generation in Nanometer-Scale Optical Coatings. *ACS Photonics* **2018**, *5*, 306−311.

(17) Sobhani, A.; Knight, M. W.; Wang, Y.; Zheng, B.; King, N. S.; Brown, L. V.; Fang, Z.; Nordlander, P.; Halas, N. J. Narrowband Photodetection in the Near-Infrared with a Plasmon-Induced Hot Electron Device. *Nat. Commun.* **2013**, *4*, No. 1643.

(18) Casalino, M.; Coppola, G.; De La Rue, R. M.; Logan, D. F. State-of-the-Art All-Silicon Sub-Bandgap Photodetectors at Telecom and Datacom Wavelengths. *Laser Photonics Rev.* **2016**, *10*, 895−921.

(19) Logan, D. F.; Jessop, P. E.; Knights, A. P. Modeling Defect Enhanced Detection at 1550 nm in Integrated Silicon Waveguide Photodetectors. *J. Lightwave Technol.* **2009**, *27*, 930−937.

(20) Mailoa, J. P.; Akey, A. J.; Simmons, C. B.; Hutchinson, D.; Mathews, J.; Sullivan, J. T.; Recht, D.; Winkler, M. T.; Williams, J. S.; Warrender, J. M.; Persans, P. D.; Aziz, M. J.; Buonassisi, T. Room-Temperature Sub-Band Gap Optoelectronic Response of Hyperdoped Silicon. *Nat. Commun.* **2014**, *5*, No. 3011.

(21) Ginley, D. S.; Bright, C. Transparent Conducting Oxides. *MRS Bull.* **2000**, *25*, 15−18.

(22) Assunção, V.; Fortunato, E.; Marques, A.; Águas, H.; Ferreira, I.; Costa, M. E. V.; Martins, R. Influence of the Deposition Pressure on the Properties of Transparent and Conductive ZnO:Ga Thin-Film

Produced by R.F. Sputtering at Room Temperature. *Thin Solid Films* **2003**, *427*, 401−405.

(23) Kim, J.; Dutta, A.; Naik, G. V.; Giles, A. J.; Bezares, F. J.; Ellis, C. T.; Tischler, J. G.; Mahmoud, A. M.; Caglayan, H.; Glembocki, O. J.; Kildishev, A. V.; Caldwell, J. D.; Boltasseva, A.; Engheta, N. Role of Epsilon-Near-Zero Substrates in the Optical Response of Plasmonic Antennas. *Optica* **2016**, *3*, 339−346.

(24) Liu, X.; Kang, J.-H.; Yuan, H.; Park, J.; Kim, S. J.; Cui, Y.; Hwang, H. Y.; Brongersma, M. L. Electrical Tuning of a Quantum Plasmonic Resonance. *Nat. Nanotechnol.* **2017**, *12*, 866.

(25) Park, J.; Kang, J.-H.; Kim, S. J.; Liu, X.; Brongersma, M. L. Dynamic Reflection Phase and Polarization Control in Metasurfaces. *Nano Lett.* **2017**, *17*, 407−413.

(26) Abb, M.; Wang, Y.; Papasimakis, N.; de Groot, C. H.; Muskens, O. L. Surface-Enhanced Infrared Spectroscopy Using Metal Oxide Plasmonic Antenna Arrays. *Nano Lett.* **2014**, *14*, 346.

(27) Traviss, D.; Bruck, R.; Mills, B.; Abb, M.; Muskens, O. L. Ultrafast Plasmonics Using Transparent Conductive Oxide Hybrids in the Epsilon-Near-Zero Regime. *Appl. Phys. Lett.* **2013**, *102*, No. 121112.

(28) Shrestha, S.; Wang, Y.; Overvig, A. C.; Lu, M.; Stein, A.; Negro, L. D.; Yu, N. Indium Tin Oxide Broadband Metasurface Absorber. *ACS Photonics* **2018**, *5*, 3526−3533.

(29) Nishimura, T.; Kita, K.; Toriumi, A. Evidence for Strong Fermi-Level Pinning Due to Metal-Induced Gap States at Metal/Germanium Interface. *Appl. Phys. Lett.* **2007**, *91*, No. 123123.

(30) Tennyson, E. M.; Garrett, J. L.; Frantz, J. A.; Myers, J. D.; Bekele, R. Y.; Sanghera, J. S.; Munday, J. N.; Leite, M. S. Nanoimaging of Open-Circuit Voltage in Photovoltaic Devices. *Adv. Energy Mater.* **2015**, *5*, No. 1501142.

(31) Spadafora, E. J.; Demadrille, R.; Ratier, B.; Grévin, B. Imaging the Carrier Photogeneration in Nanoscale Phase Segregated Organic Heterojunctions by Kelvin Probe Force Microscopy. *Nano Lett.* **2010**, *10*, 3337−3342.

(32) Garrett, J. L.; Munday, J. N. Fast, High-Resolution Surface Potential Measurements in Air with Heterodyne Kelvin Probe Force Microscopy. *Nanotechnology* **2016**, *27*, No. 245705.

(33) Hu, Y. M.; Li, J. Y.; Chen, N. Y.; Chen, C. Y.; Han, T. C.; Yu, C. C. Effect of Sputtering Power on Crystallinity, Intrinsic Defects, and Optical and Electrical Properties of Al-doped ZnO Transparent Conducting Thin Films for Optoelectronic Devices. *J. Appl. Phys.* **2017**, *121*, No. 085302.

(34) Lee, J.; Sorescu, D. C.; Deng, X. Tunable Lattice Constant and Band Gap of Single- and Few-Layer ZnO. *J. Phys. Chem. Lett.* **2016**, *7*, 1335−1340.

(35) Ye, J. D.; Gu, S. L.; Zhu, S. M.; Liu, S. M.; Zheng, Y. D.; Zhang, R.; Shi, Y. Fermi-Level Band Filling and Band-Gap Renormalization in Ga-doped ZnO. *Appl. Phys. Lett.* **2005**, *86*, No. 192111.

(36) Kim, J.; Naik, G. V.; Gavrilenko, A. V.; Dondapati, K.; Gavrilenko, V. I.; Prokes, S. M.; Glembocki, O. J.; Shalaev, V. M.; Boltasseva, A. Optical Properties of Gallium-Doped Zinc Oxide—A Low-Loss Plasmonic Material: First-Principles Theory and Experiment. *Phys. Rev. X* **2013**, *3*, No. 041037.

(37) Janotti, A.; Van de Walle, C. G. Fundamentals of Zinc Oxide as a Semiconductor. *Rep. Prog. Phys.* **2009**, *72*, No. 126501.

(38) Ellmer, K.; Bikowski, A. Intrinsic and Extrinsic Doping of ZnO and ZnO Alloys. *J. Phys. D: Appl. Phys.* **2016**, *49*, No. 413002.

(39) Scales, C.; Berini, P. Thin-Film Schottky Barrier Photodetector Models. *IEEE J. Quantum Electron.* **2010**, *46*, 633−643.

(40) Jackson, W. B.; Biegelsen, D. K.; Nemanich, R. J.; Knights, J. C. Optical Absorption Spectra of Surface or Interface States in Hydrogenated Amorphous Silicon. *Appl. Phys. Lett.* **1983**, *42*, 105−107.

(41) Mooney, J. M. The Dependence of the Schottky Emission Coefficient on Reverse Bias. *J. Appl. Phys.* **1989**, *65*, 2869−2871.

(42) Akbi, M.; Bouchou, A.; Ferhat-Taleb, M. Effects of Surface Treatments on Photoelectric Work Function of Silver−Nickel Alloys. *Vacuum* **2014**, *101*, 257−266.

(43) Vassant, S.; Hugonin, J.-P.; Marquier, F.; Greffet, J.-J. Berreman Mode and Epsilon Near Zero Mode. *Opt. Express* **2012**, *20*, 23971−23977.

(44) Campione, S.; Brener, I.; Marquier, F. Theory of Epsilon-Near-Zero Modes in Ultrathin films. *Phys. Rev. B* **2015**, *91*, No. 121408.

(45) Guo, P.; Schaller, R. D.; Ketterson, J. B.; Chang, R. P. H. Ultrafast Switching of Tunable Infrared Plasmons in Indium Tin Oxide Nanorod Arrays with Large Absolute Amplitude. *Nat. Photonics* **2016**, *10*, 267.

(46) Kim, J.; Carnemolla, E. G.; DeVault, C.; Shaltout, A. M.; Faccio, D.; Shalaev, V. M.; Kildishev, A. V.; Ferrera, M.; Boltasseva, A. Dynamic Control of Nanocavities with Tunable Metal Oxides. *Nano Lett.* **2018**, *18*, 740−746.

(47) Abb, M.; Wang, Y.; de Groot, C. H.; Muskens, O. L. Hotspot-mediated ultrafast nonlinear control of multifrequency plasmonic nanoantennas. *Nat. Commun.* **2014**, *5*, No. 4869.

(48) Capretti, A.; Wang, Y.; Engheta, N.; Dal Negro, L. Comparative Study of Second-Harmonic Generation from Epsilon-Near-Zero Indium Tin Oxide and Titanium Nitride Nanolayers Excited in the Near-Infrared Spectral Range. *ACS Photonics* **2015**, *2*, 1584−1591.

(49) Gall, D. Electron Mean Free Path in Elemental Metals. *J. Appl. Phys.* **2016**, *119*, No. 085101.